



TECHNICAL ARTICLE

Theoretical and Numerical Investigation of the Limit Strain of a 5754-O Aluminum Alloy Sheet Considering the Influence of the Hardening Law

Bolin Ma, Chunyu Yang, Xiangdong Wu, and Lihua Zhan

Submitted: 25 October 2021 / Revised: 22 December 2022 / Accepted: 30 December 2022 / Published online: 23 January 2023

This work focuses on the limit strains of 5754-O aluminum alloy sheets with consideration of the hardening law effect. Based on uniaxial tension test data, the hardening laws of Swift, Voce, LSV and Hockett–Sherby were applied to determine the mechanical properties. The fitted parameters and the Yld2000-2d yield function were introduced into the Marciniak–Kuczynski (M–K) theory to predict the forming limit curve (FLC). This prediction was not consistent with the Nakajima test results. Assessment of the effect of the hardening law on the predicted FLC indicated that the hardening law affected the yield surface evolution through the hardening rate. Afterward, an improved LSV hardening law was proposed to depict the plastic stress–strain relationship, and both the theoretical prediction and the numerical simulation verified the validity of the improved model. The results were compared with the test data, and good agreement was shown.

Keywords aluminum alloy sheet, forming limit, hardening law, M–K theory, numerical simulation, yield function

1. Introduction

Owing to their high specific strength, many aluminum alloy parts have been manufactured in the automotive and aerospace industries. Consequently, extensive studies have focused on the characteristics of aluminum alloy sheets. As a typical property of sheet metals, the forming limit curve (FLC), comprising the limit strain pairs under different strain paths or stress states, has been widely used in the sheet stamping process to represent sheet failure or fracture. Generally, the limit strain pairs of sheet metal are experimentally evaluated by stretching the sheet in different strain paths or calculated theoretically by coupling the instability criteria and material properties. The experimental data and prediction results presented in the published literature demonstrate that the forming temperature, mechanical properties, strain path, stress state, and other factors affect the forming limit of aluminum alloy sheets [1]. Many studies have focused on the formability of aluminum alloy sheets from the perspective of pre-strain, yield locus, hardening law, and plastic instability criterion.

The pre-strain was a factor affecting the FLC of the sheet metal. Graf and Hosford [2], who determined the forming limit strains of specimens pre-strained to several levels in uniaxial

tension, plane strain, and biaxial tension, found that the amount of additional plane strain deformation possible before failure depended on the effective strain during the pre-strain. Uppaluri et al. [3] extended the modified maximum force criterion by considering the pre-strain to predict the FLC and validated the theoretical model by using the experimental data determined by Graf and Hosford [2]. Cao et al. [4] combined the Marciniak–Kuczynski (M–K) approach and Karafillis–Boyce yield criterion to evaluate the forming limits of Al-2008-T4 and Al6111-T4 sheet metals under linear and nonlinear strain paths, and the predicted result was validated using the test data presented in the literature [2]. Reyes et al. [5, 6] investigated the effect of pre-strain on the FLC by applying a nonlocal criterion to detect the incipient localized necking and the through-thickness shear instability criterion. By experimentally and theoretically determining the FLC of AA5754-O, Dhara et al. [7] found that the limit strains shifted significantly depending on the amount and direction of the uniaxial pre-strain. From these studies, it can be concluded that the FLC in the strain space is dependent on the path.

The pre-strain affected the position of the FLC in the strain space, however, the work performed by Kleemola et al. [8] indicated the uniqueness of the FLC in the stress space, and that this pre-strain effect on the strain-based FLC disappeared. Fang et al. [9] showed that the strain-based FLC can be transformed into that of the stress space, and the hardening law is necessary in this transformation process. Additionally, Werber et al. [10] investigated the FLC of AA6014 by considering the pre-strain states and demonstrated that the yield criterion had a significant impact on the FLC in the stress space. A similar conclusion was also presented by Paul et al. [11]. As recommended by Stoughton et al. [12], the stress-based FLC is more suitable for sheet metal in the multi-stamping process, without concern for the strain path effect because of the uniqueness of the limit stress. However, measuring the stress components during the

Bolin Ma, Chunyu Yang, and Lihua Zhan, Light Alloy Research Institute, Central South University, Changsha 410083 Hunan, People's Republic of China; **Xiangdong Wu**, School of Mechanical Engineering and Automation, Beihang University, Beijing 100191, People's Republic of China. Contact e-mail: mabolin_csu@163.com.

sheet stamping procedure is difficult, and an appropriate yield function is an essential prerequisite for stress-based FLC [13].

There have been many studies of the influence of the yield function on the FLC. Dasappa et al. [14] predicted the FLC of a 5754 aluminum alloy sheet based on different yield functions together with the M–K approach and found that the shape of the yield function was the most dominant factor affecting the predicted result. Rocha et al. [15] evaluated the FLC of aluminum alloy 6016-T4 by coupling the M–K theory with different yield functions and hardening laws and verified the result through test data and stamping simulation. They found that the shape of the yield surface had a significant effect on the predicted FLC. The plane stress yield function, called Yld2000-2d in many studies, was proposed by Barlat et al. [16] to describe the anisotropic behavior of aluminum alloy sheets. By evaluating the effect of the microstructure on the yield loci, Iadicola et al. [17] demonstrated that the locus elongation of AA5754-O in the biaxial stretching deformation process could be fitted well by the Yld2000-2d yield criterion. Wang et al. [18] recommended the Yld2000-2d yield function to describe the mechanical behavior of a 5754-O aluminum alloy sheet and demonstrated this by comparing the deep drawing simulation results under different yield functions [19]. Kuwabara et al. [20] simulated the hole expansion process of 6016-T4 and 6016-O and found that the Yld2000-2d yield function provided proper material representations of the plastic behavior. As the above-mentioned studies demonstrated, the yield function significantly affects the theoretical prediction result, and the Yld2000-2d yield function is more suitable for aluminum alloy sheets.

Additionally, the hardening law also affects the predicted FLC of the aluminum alloy sheet [15], and many models have been developed to describe the equivalent stress–strain curve, such as the Swift, Voce, Hockett–Sherby, and Ghosh, and their combinations (e.g., LSV, Swift-Hockett/Sherby). Pham et al. [21] theoretically predicted the FLCs of AL5052-O and AL6016-T4 by applying the modified maximum force criterion (MMFC) under different hardening models and found that the Kim-Tuan model, proposed by Pham et al. [22], could improve the prediction. Gronostajski [23], who briefly reviewed different models, recommended that the choice of a proper model must be preceded by a thorough analysis of the influence of deformation conditions on the physical processes that occur in the material. By applying the M–K approach under different hardening laws and yield functions to evaluate the FLC of AA6016-T4, Butuc et al. [24] found that the FLC predicted from the Swift equation was always higher than that predicted using the Voce equation. Ding et al. [25] coupled different hardening models with the M–K theory to investigate the effects of temperature and strain rate on the predicted FLC of AA5086 and indicated that the hardening law had a significant effect on the predicted FLC. It is obvious that the hardening law yields a post-necking prediction for a tested material, and hence, the prediction result is influenced. The most appropriate hardening law for a specific material is necessary for high-precision prediction of the FLC.

The plastic instability criterion is indispensable for theoretically predicting the FLC of sheet metal. Proposed by Marciniak and Kuczynski [26], the M–K approach, in which the imperfection of a narrow band inclines at an angle φ with

the principal axis, is used as an instability criterion to calculate the limit strain pairs of sheet metals under different forming conditions [27–29]. In the M–K theory, the calculation process ended when the ratio of the major strain increment in the groove to that outside the groove increased to a critical value, and the predicted strain pair with the minimum major strain at a specific groove orientation was treated as the limit strain. Although the FLC predicted by applying the M–K approach strongly depended on groove orientation φ , imperfection coefficient f_0 , and the critical value, extensive studies based on the M–K approach were conducted to investigate the formability of aluminum alloy sheets. By applying the M–K theory with an elastic–plastic constitutive model including mixed isotropic-distortional hardening, Aretz [30] predicted the FLC of the AA7018-T6 sheet metal and demonstrated the impact of distortional hardening on localized necking predictions. Yoshida et al. [31] discussed the influence of the texture of an aluminum alloy sheet on the limit strains by applying the M–K approach and a generalized Taylor-type polycrystal model. Chiba et al. [32] investigated the FLC of AA1100-H24 by applying the M–K model to compare the prediction results determined from phenomenological and crystal plasticity theories. By coupling the M–K theory and the Yld2000-2d yield function, Wang et al. [33] studied the effect of pre-strain on the strain-based and stress-based FLCs of a 5754-O aluminum alloy sheet. Yue et al. [34] determined the stress-based FLC of AL7020 by applying the M–K approach and found that the FLC in the stress space and the failure criterion using the damage mechanics model can better reproduce the local crack initiation in sheet metal forming.

To avoid the complicated process of solving the highly nonlinear equilibrium and related compatibility equations in the M–K approach, some studies focused on the finite element (FE) M–K approach have also been conducted to predict the FLC of aluminum alloy sheets. Banabic et al. [35] evaluated the FLC of AA5182-O by applying the FE M–K approach, the MMFC criterion, the Swift's diffuse method, and the Hill's localized necking approach and confirmed the validity of the finite element M–K model. Chu et al. [36] investigated the FLC of AA5086 by considering the temperature and strain rate and indicated that the FE M–K model can be effective for predicting sheet metal formability. Zhang et al. [37] reported an approach to evaluate the sheet formability by combining a tensile test with the FE M–K model. Ma et al. [38, 39] focused on developing the FE M–K approach for predicting the FLC of AA5754-O and evaluating the influence of the pre-strain on the strain-based FLC.

In this study, the M–K approach and the Yld2000-2d yield function were coupled to evaluate the effect of the hardening law on the predicted FLC, and an improved hardening law for 5754-O aluminum alloy sheet was proposed. First, the Nakajima test was performed to determine the limit strains, and the experimental data from the uniaxial tensile test were fitted using different hardening laws to evaluate the mechanical properties. Then, the M–K approach and the Yld2000-2d yield function were applied to predict the FLC and determine the effect of the hardening law on the prediction result. Finally, an improved LSV hardening law was proposed to predict the forming limit, and good agreement between the test data and theoretical FLC was presented.

2. Experimental Details

2.1 The Nakajima Test

The Nakajima test is typically performed to determine the experimental limit strain pairs of sheet metals. The material used in this study was 5754-O aluminum alloy sheet with a thickness of 1.5 mm. The FLC specimens were prepared according to the sizes given in Reference [40] and are shown in Fig. 1. Before the Nakajima test, circular grids with a diameter of 2.5 mm were printed on the specimen surface, and then, the specimen surface was treated with molybdenum disulfide grease to provide good lubrication conditions. During the test, the specimen was fixed on the die and stretched using a hemispherical rigid punch with a diameter of 100 mm. The stretching process ended when the forming force reached its maximum value. Ozturka et al. [41] demonstrated that the lubrication affects the position of the sheet failure and the location of the limit strain pair in the strain space. However, friction between the rigid punch and the deformed sheet is inevitable. Thus, one specimen with a size of 180 × 180 mm (marked as 180 mm-2) was stretched by applying the hydraulic forming method to determine the limit strain pair in the equi-biaxial strain state. The deformed specimens are shown in Fig. 2.

The punch displacement and forming force during the expansion process were acquired using a grating-scale displacement sensor and a load sensor, respectively. The experimental punch displacement–force curves of some specimens are shown in Fig. 3. It shows that the maximum dome heights for specimens with sizes of 20, 80, 100, and 180 mm were 20, 30, 28, and 35 mm, respectively.

After the Nakajima test, the size of each deformed grid near the failure was measured. The failure region was located near the centerline of the deformed specimen, and the distance between the measured grid and the failure region did not exceed the size of one grid. Considering the grid line width, the inner diameter, outside diameter, and pitch diameter of each grid were measured (diagramed in Fig. 4), and the average value

was used to calculate the forming limit strain pairs [27, 29]. The strain measurement system is shown in Fig. 4. The measured results are shown in Fig. 5. The measured major limit strain under the plane strain state and the equi-biaxial tension strain are 0.23 and 0.31, respectively.

2.2 Uniaxial Tensile Test

Based on the national test standard GB/T228-2002, a uniaxial tensile test was conducted using an INSTRON 5582 machine, and the strain during the deformation process was measured using a YYU-10/50 extensometer with an accuracy of 2 mV/V. Specimens at 0°, 45°, and 90° with respect to the rolling direction were prepared, and uniaxial tensile tests along each direction were performed three times. During the test procedure, the anisotropy R -value, defined as the ratio of the strain along the width to the strain along the thickness, was measured when the elongation reached 10% [37, 42]. The strains along the length and width directions were simultaneously measured using two extensometers. The R -value and Young's modulus E were fitted using Origin software. During the Young's modulus fitting process, stress–strain data pairs with stresses below 90 MPa were used (near the yield point). For each specimen, the yield stress σ_0 and the fitted data are shown in Table 1. The plastic stress–strain curves determined from the uniaxial tensile tests are shown in Fig. 6.

In this study, the following four hardening models were utilized to fit the experimental plastic stress–strain curve, and the fitted parameters in each model are listed in Table 2. In Eqs. (1)–(4), the symbols σ_e and ε_e indicate the equivalent stress and the equivalent strain, respectively.

$$\text{Swift model} \quad \sigma_e = K(\varepsilon_e + \varepsilon_0)^n \quad (\text{Eq 1})$$

$$\text{Voce model} \quad \sigma_e = \sigma_0 + K(1 - \exp(-A\varepsilon_e)) \quad (\text{Eq 2})$$

$$\text{Hockett - Sherby model} \quad \sigma_e = \sigma_0 + A(1 - \exp(-B\varepsilon_e^n)) \quad (\text{Eq 3})$$

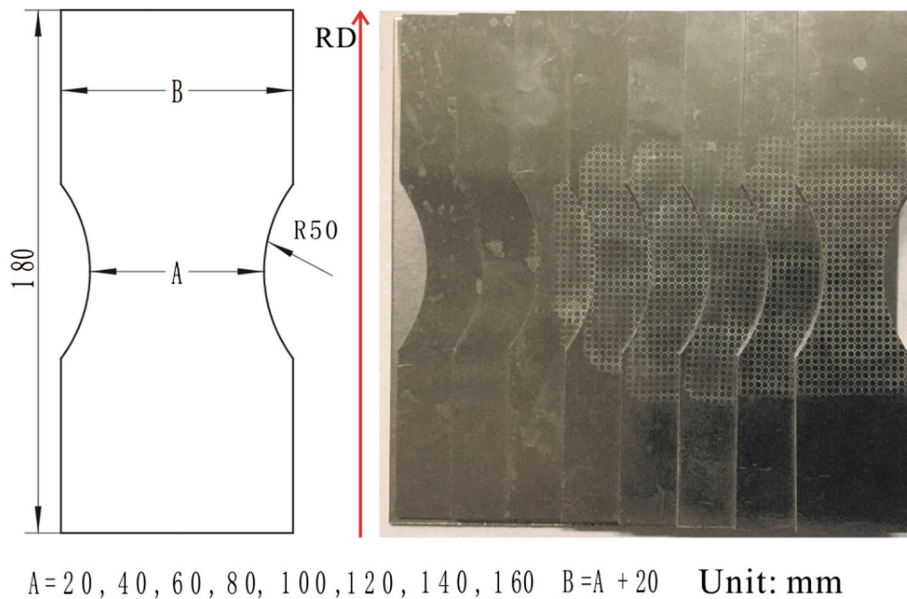


Fig. 1 Size of the FLC specimen before the test

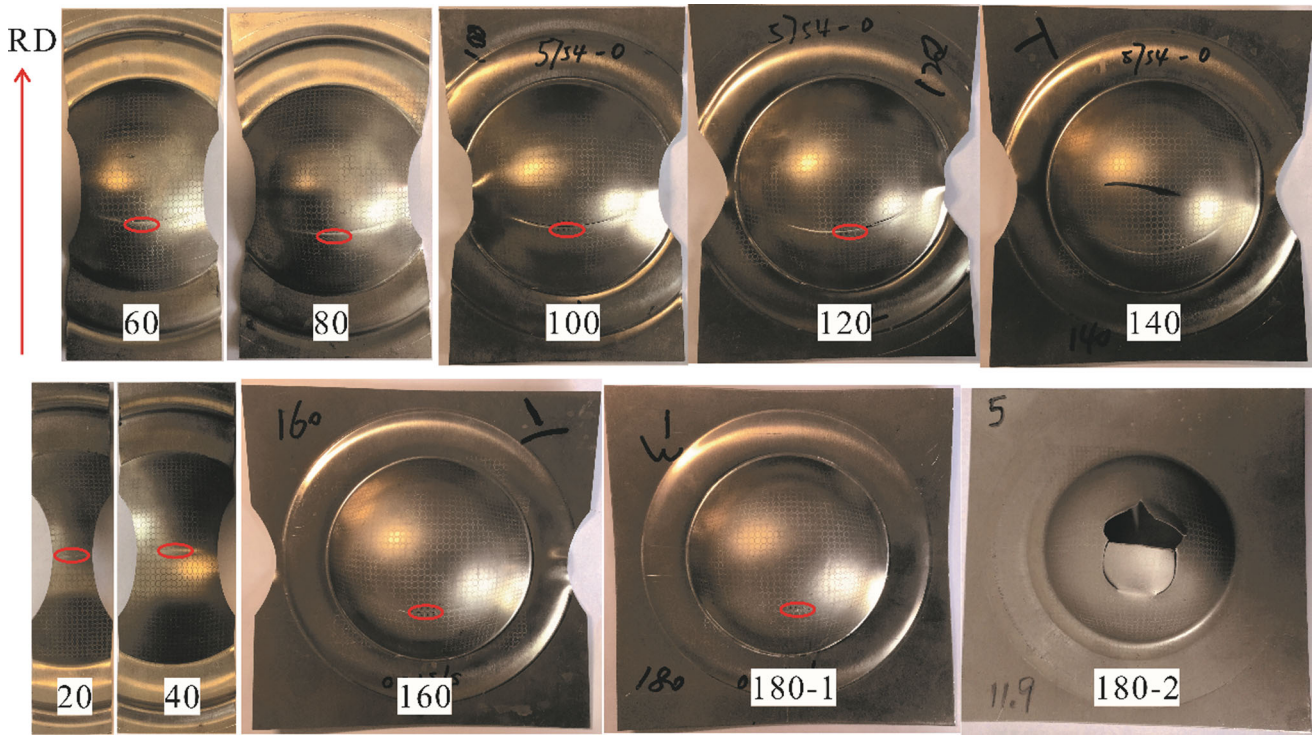


Fig. 2 Deformed specimens after the test

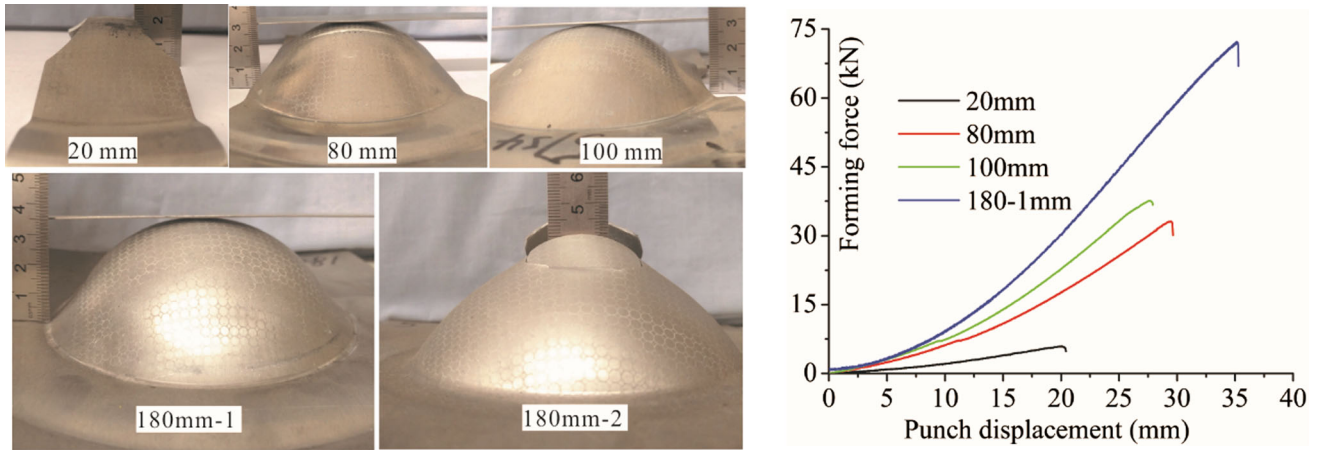


Fig. 3 Displacement-force curves of some specific specimens

$$\text{LSVmodel } \sigma_e = k_1 * \sigma_{\text{Swift}} + k_2 * \sigma_{\text{Voce}} \quad (\text{Eq 4})$$

In addition, σ_{Swift} and σ_{Voce} indicate the equivalent stresses fitted by the Swift and Voce models, respectively.

The fitted curve of each hardening model was plotted and compared with the test data as shown in Fig. 7. It can be seen that each hardening model fits well with the test data when the plastic strain is less than 0.2. However, the difference between the predicted stresses from each hardening law is significant when the plastic strain exceeds 0.2. This difference in predictions under large strain conditions shown in Fig. 7 makes it difficult to determine which hardening law is appropriate for describing the stress-strain relationship [43]. Many studies have predicted the stress-strain relationship under large strain conditions by applying different methods. However, the

published literature shows that these methods are not yet fully verified in terms of both the theoretical basis and measurement techniques [44–46]. Therefore, research on the hardening law under large strain conditions is also needed, which provides an opportunity to validate the hardening law through FLC prediction.

3. Forming Limit Curve (FLC) Theoretical Prediction

3.1 Yield Function

Proposed and recommended by Barlat et al. [16], the non-quadratic anisotropic yield criterion, called Yld2000-2d, is

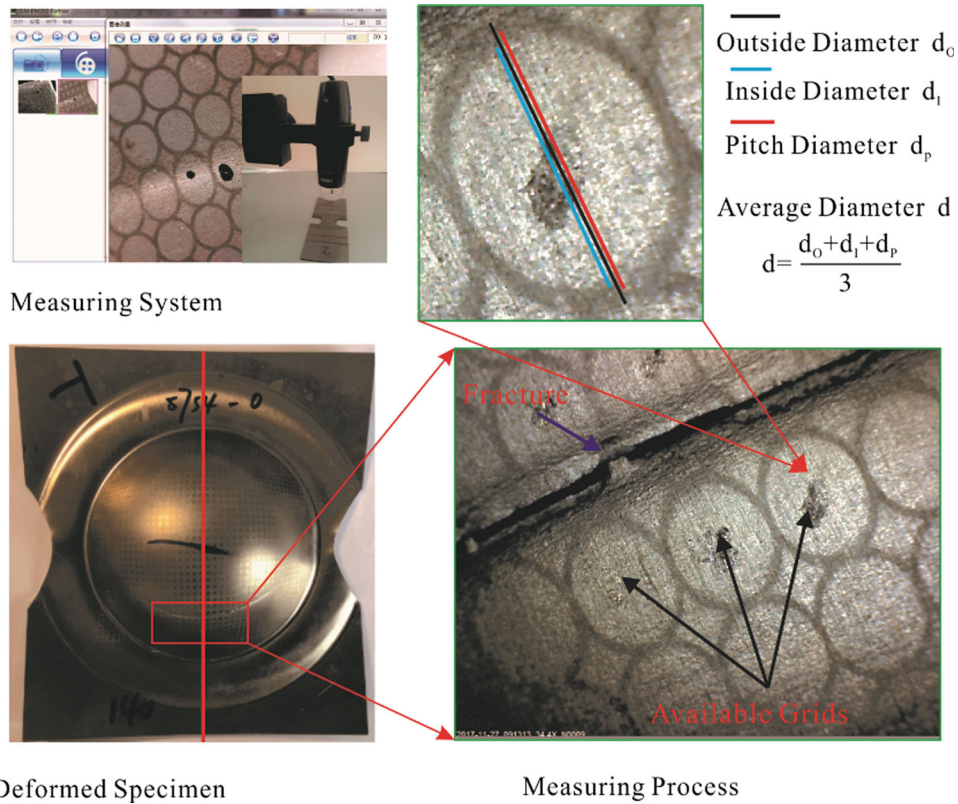


Fig. 4 Strain measurement system

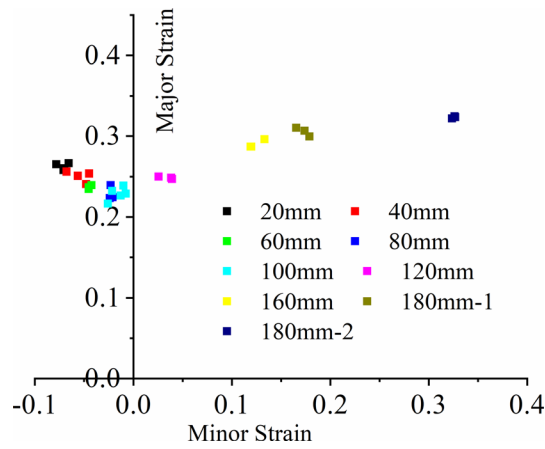


Fig. 5 Measured limit strain pairs in the strain space

Table 1 The fitted data of each specimen

	0°			45°			90°			Average value
	No.1	No.2	No.3	No.1	No.2	No.3	No.1	No.2	No.3	
<i>R</i>	0.785	0.793	0.788	0.713	0.725	0.723	0.789	0.796	0.787	0.766
<i>E</i> (GPa)	66.21	69.41	66.38	59.97	56.51	59.55	58.64	64.995	64.32	62.88
σ_0 (MPa)	116.42	116.25	116.91	116.73	119.82	117.51	121.06	120.42	120.68	118.39

suitable for predicting the yield behavior in the plane stress state; thus, this yield function was applied in this study. It was expressed as

$$\phi = \phi' + \phi'' = 2\sigma_c^m \quad (\text{Eq 5})$$

where

$$\begin{cases} \phi' = |Y'_1 - Y'_2|^m \\ \phi'' = |2Y''_2 + Y''_1|^m + |2Y''_1 + Y''_2|^m \end{cases} \quad (\text{Eq 6})$$

Y'_i and Y''_j ($i, j = 1, 2$) are the principal values of matrices \mathbf{X}' and \mathbf{X}'' , respectively, and are formulated as follows:

$$\begin{cases} Y'_i = \frac{1}{2}(X'_{11} + X'_{22} \pm \sqrt{(X'_{11} - X'_{22})^2 + 4X'_{12}{}^2}) \\ Y''_i = \frac{1}{2}(X''_{11} + X''_{22} \pm \sqrt{(X''_{11} - X''_{22})^2 + 4X''_{12}{}^2}) \end{cases} \quad (\text{Eq 7})$$

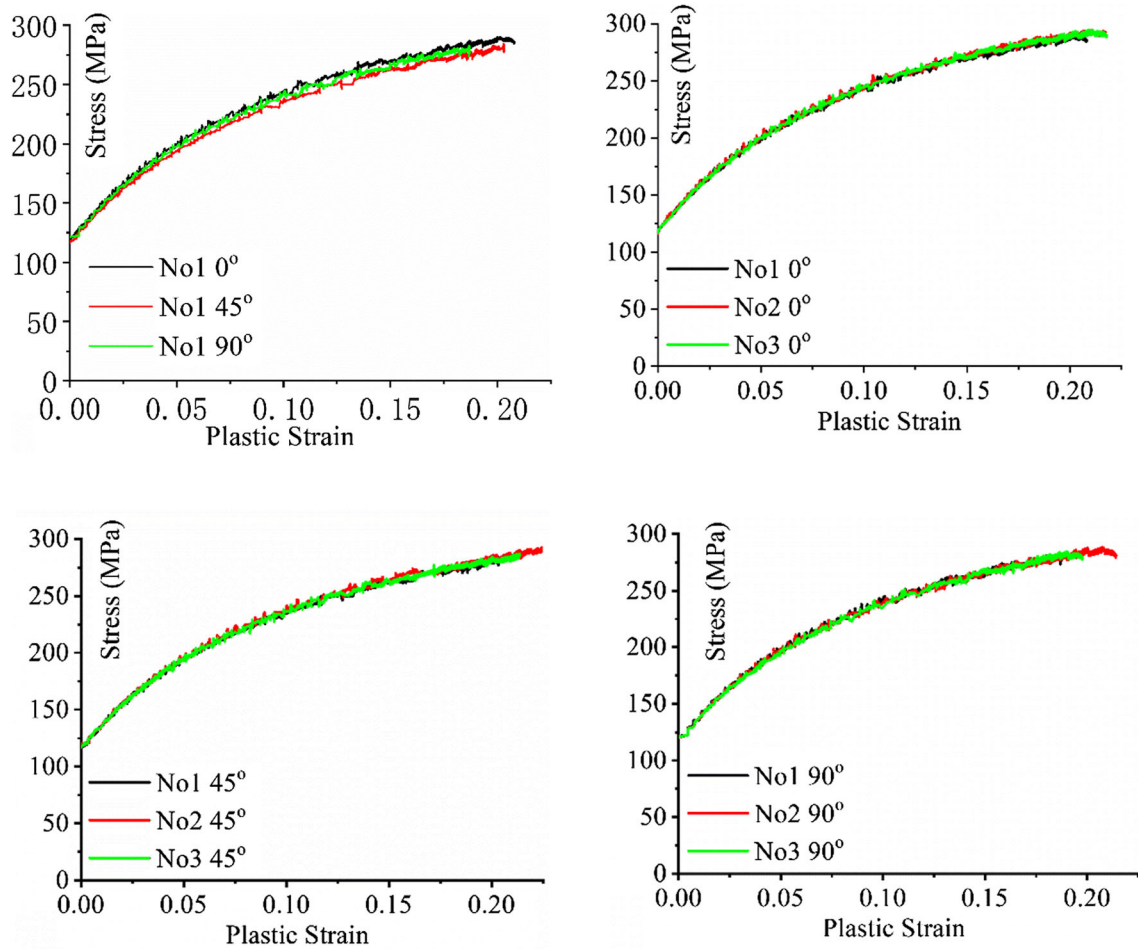


Fig. 6 Plastic stress–strain data from the uniaxial tensile test

Table 2 The fitted parameters in each hardening law

Symbols	0°			45°			90°			AverageValue
	No.1	No.2	No.3	No.1	No.2	No.3	No.1	No.2	No.3	
Swift model $\sigma_e = K(\epsilon_e + \epsilon_0)^n$										
K(MPa)	468.943	471.819	474.665	459.371	456.145	454.406	470.697	459.675	466.984	464.745
$\epsilon_0 \cdot 10^2$	0.929	0.920	0.960	1.009	0.894	0.939	1.000	0.902	1.007	0.951
n	0.301	0.301	0.305	0.306	0.298	0.300	0.309	0.299	0.308	0.303
R-Square*10 ²	99.73	99.76	99.73	99.81	99.74	99.79	99.78	99.73	99.75	
Voce model $\sigma_e = \sigma_0 + K*(1-\exp(-A*\epsilon_e))$										
σ_0 (MPa)	119.623	120.145	119.768	116.973	117.726	117.736	118.255	118.177	118.443	118.538
K(MPa)	186.297	188.815	189.464	180.470	184.911	183.892	179.732	183.187	185.054	184.647
A	11.069	10.940	10.852	10.899	10.670	10.513	11.477	10.995	10.656	10.897
R-Square*10 ²	99.91	99.915	99.93	99.90	99.89	99.90	99.87	99.83	99.85	
Hockett–Sherby model $\sigma_e = \sigma_0 + A*(1-\exp(-B*\epsilon_e^n))$										
σ_0 (MPa)	117.378	117.706	117.824	114.330	115.005	114.714	116.157	115.153	115.727	115.999
A(MPa)	199.225	203.472	201.129	198.425	199.649	201.674	193.237	200.320	201.781	199.879
B	8.623	8.036	8.473	7.539	7.804	7.294	8.623	7.687	7.631	7.968
n	0.923	0.913	0.930	0.900	0.910	0.896	0.923	0.899	0.908	0.911
R-Square*10 ²	99.93	99.94	99.95	99.93	99.91	99.93	99.885	99.87	99.88	
LSV model $\sigma_e = k_1*\sigma_{Swift} + k_2*\sigma_{Voce}$										
k ₁	0.238	0.278	0.238	0.328	0.301	0.340	0.315	0.327	0.337	0.3
k ₂	0.780	0.744	0.784	0.659	0.695	0.650	0.688	0.674	0.663	0.704
R-Square*10 ²	99.93	99.93	99.94	99.93	99.92	99.93	99.88	99.88	99.88	

The elements of \mathbf{X}' and \mathbf{X}'' are obtained using the linear transformation of the stress components, as shown in Eq. (8).

$$\begin{cases} \mathbf{X}' = \mathbf{L}'\sigma \\ \mathbf{X}'' = \mathbf{L}''\sigma \end{cases} \quad (\text{Eq 8})$$

where

$$\begin{bmatrix} L'_{11} \\ L'_{12} \\ L'_{21} \\ L'_{22} \\ L'_{66} \end{bmatrix} = \begin{bmatrix} 2/300 \\ -1/300 \\ 0 - 1/30 \\ 02/30 \\ 001 \end{bmatrix} \begin{bmatrix} \alpha_1 \\ \alpha_2 \\ \alpha_7 \end{bmatrix} \quad (\text{Eq 9})$$

$$\begin{bmatrix} L''_{11} \\ L''_{12} \\ L''_{21} \\ L''_{22} \\ L''_{66} \end{bmatrix} = \frac{1}{9} \begin{bmatrix} -228 - 20 \\ 1 - 4 - 440 \\ 4 - 4 - 410 \\ -282 - 20 \\ 00009 \end{bmatrix} \begin{bmatrix} \alpha_3 \\ \alpha_4 \\ \alpha_5 \\ \alpha_6 \\ \alpha_8 \end{bmatrix} \quad (\text{Eq 10})$$

Regarding the Yld2000-2d yield function, the parameter σ is the Cauchy stress tensor, and the value of parameter m in Eqs. (5) and (6) is set to 8 because the 5754-O aluminum alloy sheet is a material with a face-centered cubic (FCC) structure. The eight independent anisotropy coefficients, α_1 – α_8 , were determined by applying the numerical approach presented by Barlat et al. [16], and the values of each parameter are listed in Table 3. The yield stress and the R_b value under the equi-biaxial tension state are 117.2 MPa and 0.959, respectively. The biaxial tensile equipment used in this study is described in our previous work [47].

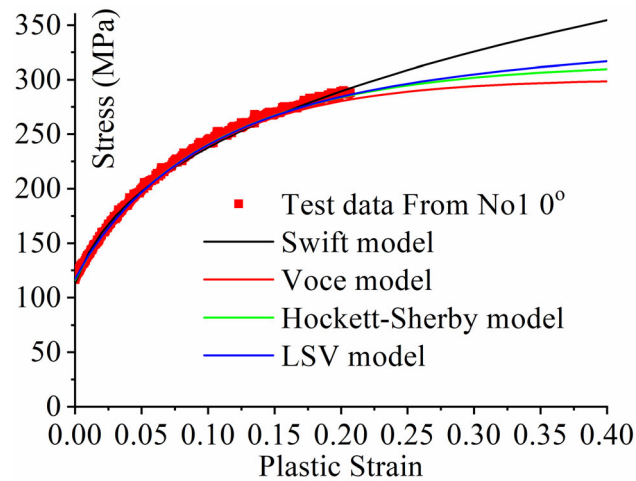


Fig. 7 Comparison among the fitted curve and the test data

Table 3 Values of the parameters in the Yld2000-2d yield function

α_1	α_2	α_3	α_4	α_5	α_6	α_7	α_8
1.02664	0.90663	0.97341	0.98256	1.00252	0.97341	0.96304	1.03595

3.2 M–K Approach

As proposed by Marciniak and Kuczynski [26], the M–K model has been widely used to predict the forming limit of sheet metals. As shown in Fig. 8, the postulate of the M–K model is a groove (marked as b) inclined at angle φ_0 with the principal axis, and the imposition of boundary conditions is as follows: geometrical imperfection (Eq. (11)), equilibrium of forces (Eq. (12)), and deformation compatibility (Eq. (13)).

$$f_0 = t_0^b / t_0^a \quad (\text{Eq 11})$$

$$\begin{cases} \sigma_{nn}^a t^a = \sigma_{nn}^b t^b \\ \sigma_{nt}^a t^a = \sigma_{nt}^b t^b \end{cases} \quad (\text{Eq 12})$$

$$dc_{tt}^a = dc_{tt}^b \quad (\text{Eq 13})$$

In the prediction procedure of the M–K theory, the major strain increment $d\varepsilon$ ($\rho^a = d\varepsilon/d\varepsilon$) under a specific stress state (σ/σ) is loaded on the region outside the groove, and then, the other strain increments, strain components, and stress components outside the groove can be solved by applying the flow rule. Subsequently, the parameters in the groove, that is, the stress states (σ/σ , σ/σ) and major strain increment $d\varepsilon$, were calculated by applying Eqs. (12) and (13). The prediction process ended when the ratio of the major strain increment in the groove to that outside the groove reached a critical value ($d\varepsilon/d\varepsilon > 7$).

This procedure was repeated for each initial groove orientation φ_0 , and the groove orientation φ was updated using Eq. (14) during the prediction procedure. The limit strain pairs under different initial groove conditions were solved, and the strain pair with the minimum major strain was treated as the predicted limit strain.

$$\tan(\varphi + d\varphi) = \tan\varphi \frac{1 + dc_{11}^a}{1 + dc_{22}^a} \quad (\text{Eq 14})$$

3.3 Prediction Results

The M–K theory and the Yld2000-2d yield function were employed to predict the FLCs under different hardening laws. In this study, the principal strain increment outside the groove and the critical value were 0.00005 and 7, respectively. It is known that the predicted limit strain increases with an increase in the imperfection coefficient f_0 . However, this increasing trend changes as f_0 increases to a critical value, as shown in Fig. 9. The predicted limit strains on the left-hand side of the FLC and the plane strain condition hardly increase. Figure 9 shows that the predicted limit strains under the plane strain condition based on the Hockett–Sherby, Voce, and LSV models are smaller than the experimental results (see Fig. 5). This demonstrates that the predicted limit strains cannot be made to agree with the experimental data by adjusting the value of the imperfection coefficient f_0 .

However, for the Swift model, the limit strain under the plane strain condition was predicted when the imperfection coefficient f_0 was set to 0.991. The predicted FLC based on each hardening law is shown and compared with the test data in

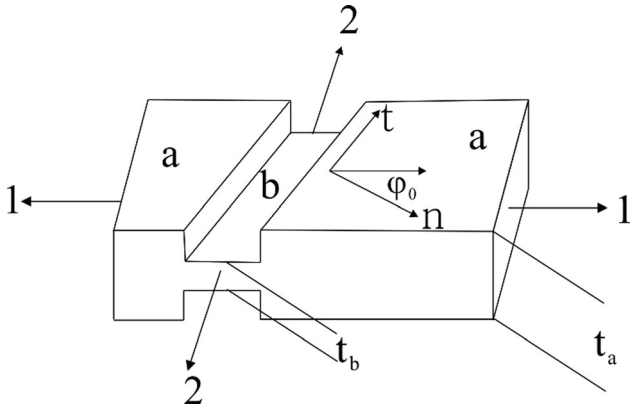


Fig. 8 M-K model

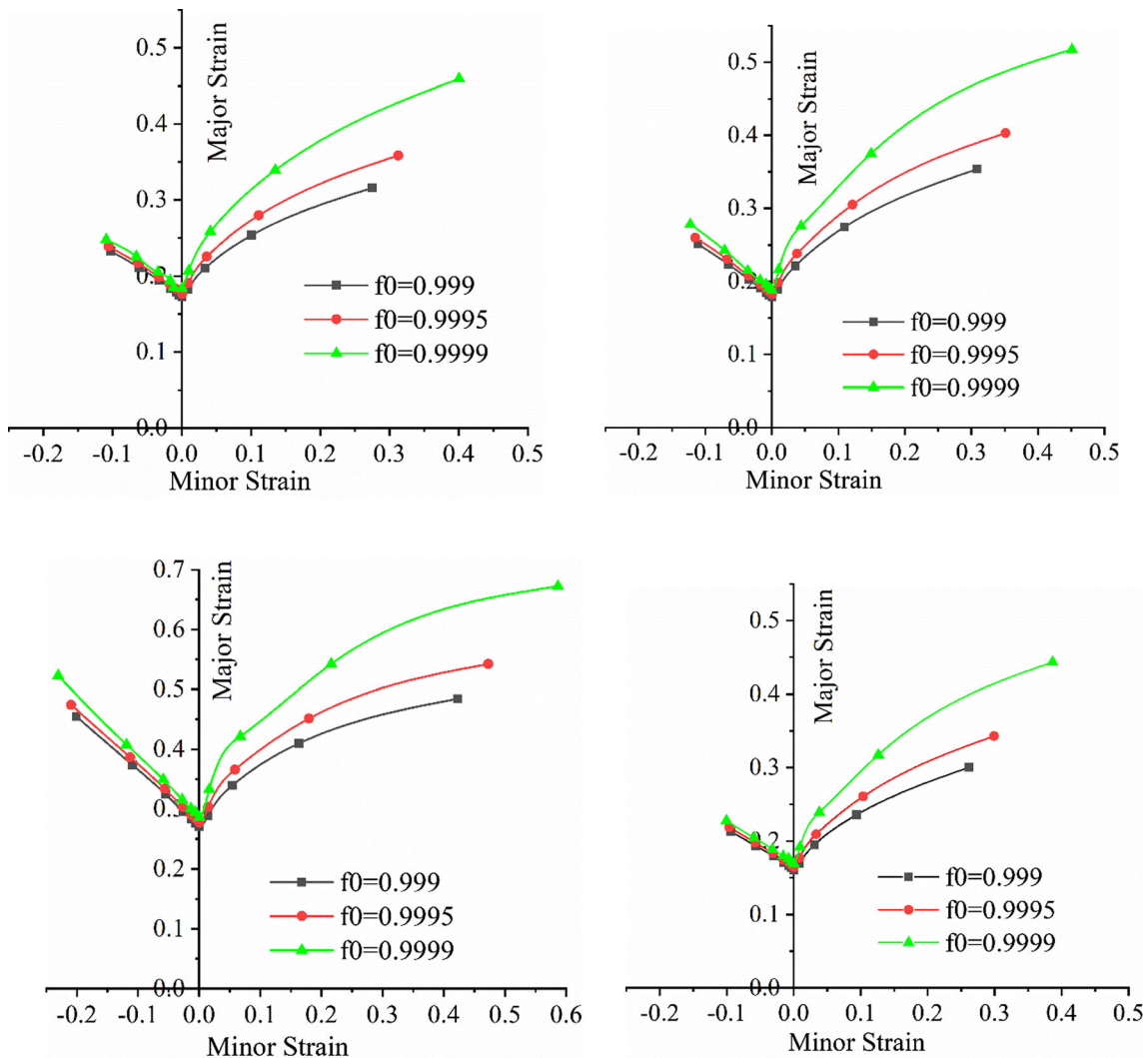


Fig. 9 Imperfection coefficient effect on the predicted FLC

Fig. 10. This demonstrates that the hardening law significantly affects the predicted FLC.

To clarify the effect of the hardening law on the predicted limit strain pair, the imperfection coefficient, $f_0 = 0.995$, and the principal strain increment, $d\epsilon = 0.00005$, were applied to calculate the limit strain pair. As shown in Fig. 11, a significant difference exists between the predicted FLCs for each hardening law.

According to the flow rule, the direction of the plastic strain rate is determined by the normal direction of the yield surface; thus, the equivalent strain increment $d\epsilon_e$ depends only on the stress ratio $\alpha = \sigma_{22}/\sigma_{11}$ and the major strain increment $d\epsilon_{11}$. Owing to the hardening rate, $H = d\sigma_e/d\epsilon_e$, the hardening law affects the equivalent stress increment $d\sigma_e$; consequently, the yield surface evolves at different rates. The hardening rate H was evaluated from the derivative of the hardening law Eqs. (1)–(4), and its evolution with the equivalent strain is shown in Fig. 12. The difference in the hardening rate determined from each hardening law is significant.

To explain how the hardening rate affects the prediction result, the original M-K instability criterion, which ignores the groove orientation, was utilized. Because $d\epsilon = d\epsilon$ and $f_0 < 1$, the $d\epsilon > d\epsilon$ relationship is valid during the iterative process.

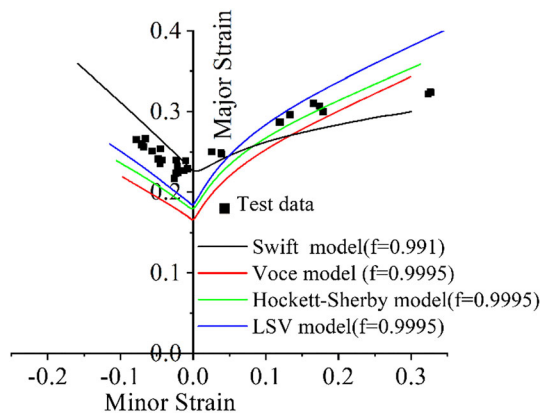


Fig. 10 Predicted FLCs and the Nakajima test results ($d\varepsilon = 0.00005$)

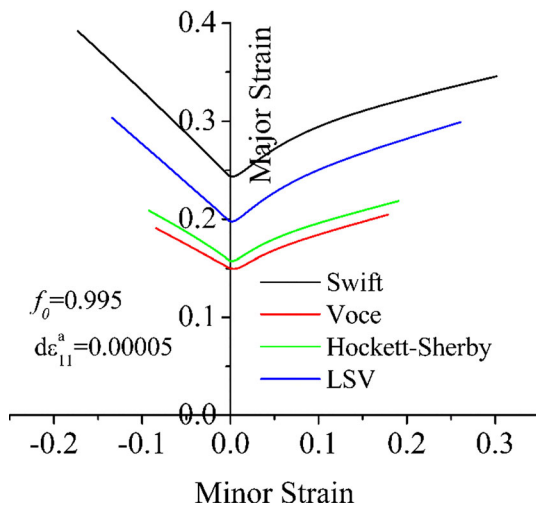


Fig. 11 Predicted FLCs from each hardening law

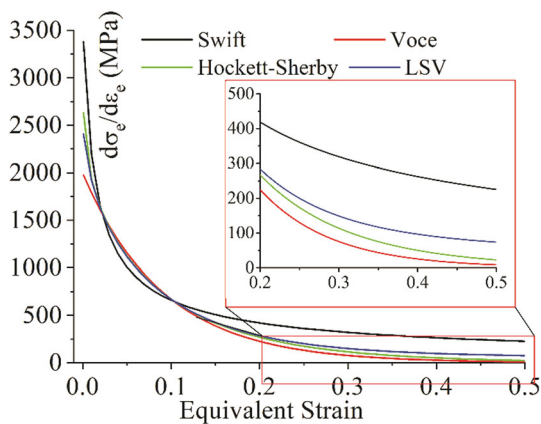


Fig. 12 Relationship between equivalent strain ε_e and $d\sigma_e/d\varepsilon_e$

Owing to the force equilibrium, the major strain increment, $d\varepsilon$, in the groove increases rapidly; consequently, the strain state ($d\varepsilon/d\varepsilon$) in the groove gradually approaches a plane strain state, and a large value of $d\varepsilon/d\varepsilon$ is obtained.

Because of the flow rule, the equivalent strain increment $d\varepsilon_e$ depends on the major strain increment, $d\varepsilon_{II}$, and the stress ratio, α . For the two hardening laws, A and B, based on the

assumption that $H_B > H_A$, the $d\sigma > d\sigma$ relationship can be confirmed at the beginning of the calculation. This indicates that the degree of yield surface expansion under hardening law B is more noticeable (shown in Fig. 13). In the next iterative process, the stress ratios in the groove based on hardening laws A and B are $\alpha^{b-A} = (\sigma + d\sigma)/(\sigma + d\sigma)$ and $\alpha^{b-B} = (\sigma + d\sigma)/(\sigma + d\sigma)$, respectively.

As the equivalent stress increment, $d\sigma$ is larger than $d\sigma$, $d\sigma$ is greater than $d\sigma$. At the beginning of the calculation procedure, for the uniaxial tensile stress state, the values of parameters $d\sigma$ and $d\sigma$ approach zero; therefore, $\alpha^{b-B} < \alpha^{b-A}$ is valid. For the equi-biaxial tensile stress state, the values of $d\sigma$ and $d\sigma$ approach $d\sigma$ and $d\sigma$, respectively, resulting in $\alpha^{b-B} > \alpha^{b-A}$.

Based on this analysis, the stress evolution under different stress conditions is shown in Fig. 13. The strain state in the groove under the condition of applying hardening law A is closer to the plane strain state (red line in Fig. 13); consequently, a small limit strain is predicted. Therefore, the essence of the hardening law effect on the FLC is the hardening rate H . A smaller value of the parameter H results in a lower position of the predicted FLC in the strain space, that is, the position of the FLC in the strain space in Fig. 11 corresponds to the value of H in Fig. 12.

4. Model Correction and Validation

4.1 Forming limit curve

As shown in Fig. 11 and 12, parameter H affects the forming limit. The limit strain pair under the plane strain condition can be predicted by applying the Swift model (shown in Fig. 10), whereas the other models fail because of a small H value. As the equivalent strain increases, the Swift model fails to predict the limit strain under the biaxial tension strain state owing to the larger value of H . The combination model, such as the LSV model, changes the parameter H (shown in Fig. 12 and 14). Therefore, considering this principle, the LSV model was modified to Eq. (15) to increase the hardening rate in the plane strain state and decrease the hardening rate in the biaxial tensile strain state, where the parameter K was fitted through the experimental data shown in Fig. 6 and its average value was -2 , k_1 and k_2 were 0.3 and 0.704, respectively (see the LSV model in Table 2). Based on the derivative of function σ_e which is expressed in Eq. (15), the hardening rate H can be expressed as Eq. (16).

$$\sigma_e = (k_1 + e^{K\varepsilon_e}) * \sigma_{\text{Swift}} + (k_2 - e^{K\varepsilon_e}) * \sigma_{\text{Voce}} \quad (\text{Eq. 15})$$

$$H = \frac{\partial \sigma_e}{\partial \varepsilon_e} = H_{\text{LSV}} + e^{K\varepsilon_e} (H_{\text{Swift}} - H_{\text{Voce}}) + K e^{K\varepsilon_e} (\sigma_{\text{Swift}} - \sigma_{\text{Voce}}) \quad (\text{Eq. 16})$$

As shown in Fig. 14, the plastic stress–strain curve determined from Eq. (15) describes the flow stress well, and the H value of this improved LSV model also changes. With the imperfection coefficient as $f_0 = 0.998$ and the major strain increment as $d\varepsilon = 0.00005$, the FLC was predicted, as shown in Fig. 15. The modified LSV model can be utilized to predict the FLC with a higher accuracy.

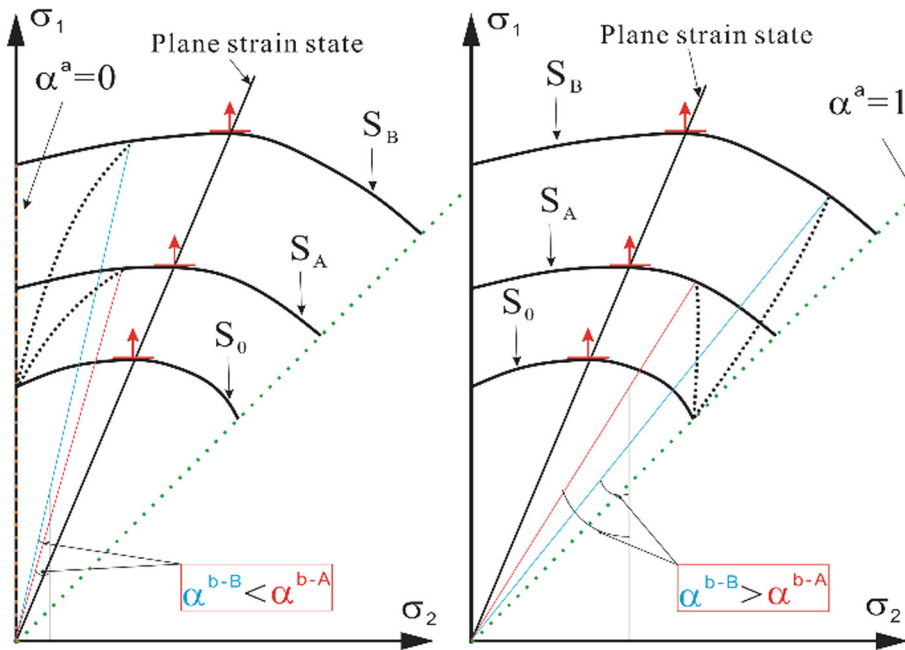


Fig. 13 Strain state evolution of the groove region under different hardening laws (left: tensile stress state; right: equi-biaxial tensile stress state)

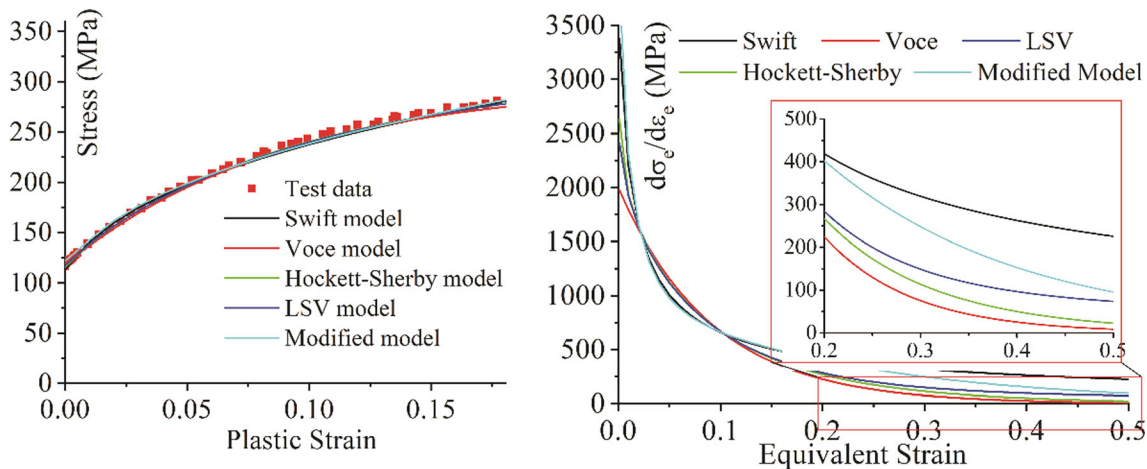


Fig. 14 Fitted plastic stress–strain curve and the value of parameter H of the modified hardening law

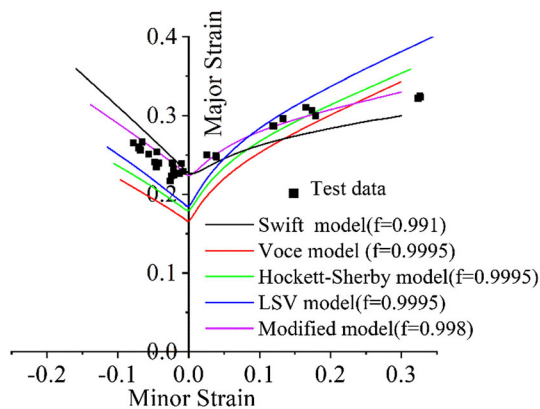


Fig. 15 Comparison between the prediction results and the experimental data

4.2 Numerical Simulation

The simulation of the stretching sheet metal under equal-biaxial strain conditions was conducted using Abaqus software (version 6.14) to investigate the hardening law effect and validate the modified LSV model. According to the mesh sensitivity investigation presented in the literature [41], the size of the mesh, typed as S4R, in the simulation was set to 2.5 mm, and a general static analysis procedure was applied with a friction coefficient of 0.03. Based on the Yld2000-2d yield function, the Voce, Swift, and modified LSV hardening laws were utilized by implementing the UMAT subroutines. During the simulation, the sheet metal was fixed on the die by applying a holding force of 50 kN and then stretched using a rigid punch.

Figure 16 shows the numerical specimen deformation for the same simulation time (stretching time: 32.29 s). Moreover, the punch displacement and the forming force were extracted from the simulation results, and each simulated punch displacement–

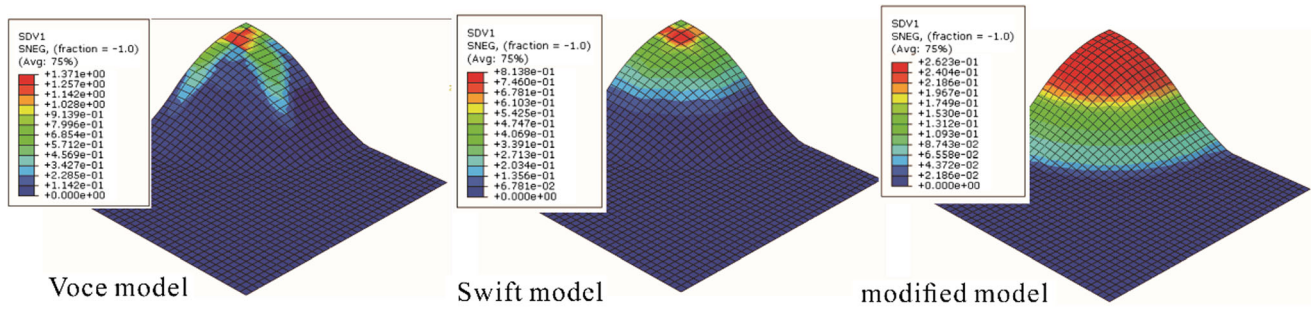


Fig. 16 Stretching results under different hardening laws (stretching time: 32.29 s)

force curve was plotted, as shown in Fig. 17. These two figures demonstrate that the hardening law strongly affects the numerical stretching process and the strain distribution. As shown in Fig. 16, the simulated strain distribution based on the modified LSV model is more uniform; hence, the corresponding punch displacement in Fig. 17 is larger. The simulation results in Fig. 17 display that the modified LSV model is suitable.

Figure 16 shows that the simulated strain distribution based on the Voce model is close to that based on the Swift model; consequently, the two simulated displacement–force curves shown in Fig. 17 are close in the uniform deformation stage. Owing to the small hardening rate H , the forming force based on the Voce model is the smallest (in Fig. 12). The maximum forming forces from the Swift and the modified LSV models approach the actual value, but the modified LSV model is more suitable for depicting the actual forming displacement–force curve.

To show the influence of the hardening law on the limit strain, the method of comparing the major strain increments of the necked element and its adjacent element was applied to determine the numerical limit strain pair [48]. In this study, parameter B is defined in Eq. (17). When necking occurs, it centralizes the deformation in the necked element, resulting in an increase in the value of parameter B .

$$B = d\epsilon_{\text{necked}}^1 / d\epsilon_{\text{adjacent}}^1 \quad (\text{Eq. 17})$$

The limit strain data were extracted from the simulation results, and parameter B was calculated and is shown in Fig. 18. The results indicate that the value of parameter B increases sharply when necking occurs. In this study, when parameter B is greater than 10, the strain of the element adjacent to the necked element is regarded as the limit strain. For Voce, Swift, and the modified LSV model, Fig. 18 shows that the times when necking occurs are 22.93, 29.45 and 44.26 s, respectively. The deformation based on each hardening law is shown in Fig. 19, which demonstrates that the hardening law affects the position of the necked element and that the simulation result from the modified LSV model is consistent with the test result (shown in Fig. 20).

This instability criterion is applied to determine the simulated strain path and compare with the test data, as presented in Fig. 20. This indicates that the hardening law influences the strain path and the limit strain and that the simulated limit strain based on the modified LSV model is close to the experimental data. The position of the limit strain under the equal-biaxial strain condition from the Swift model is the lowest, and this numerical result is consistent with the theoretical result presented in Fig. 15.

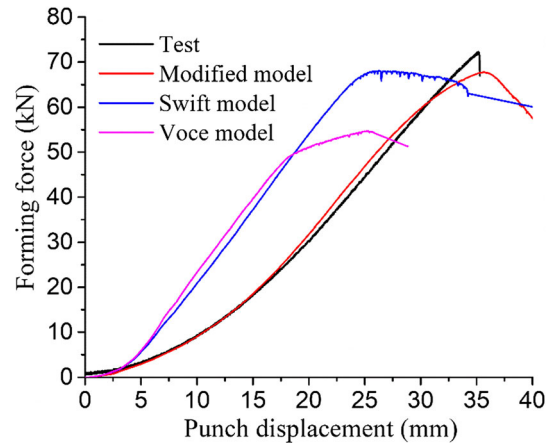


Fig. 17 Comparison between the experimental displacement–force curve and numerical curves

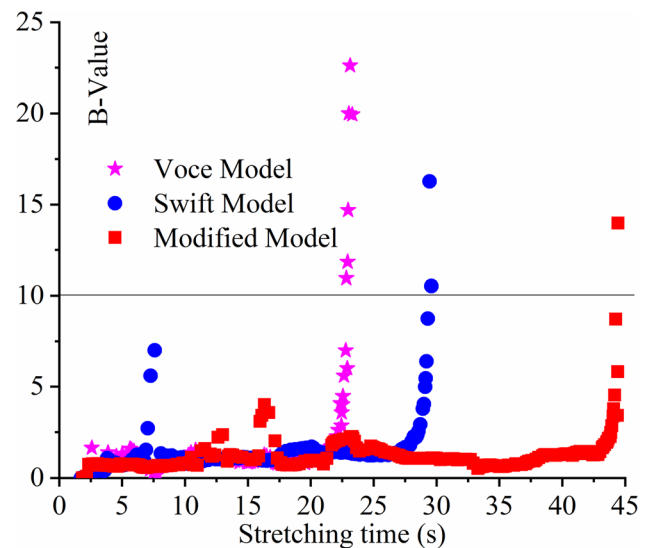


Fig. 18 B-value under different hardening laws

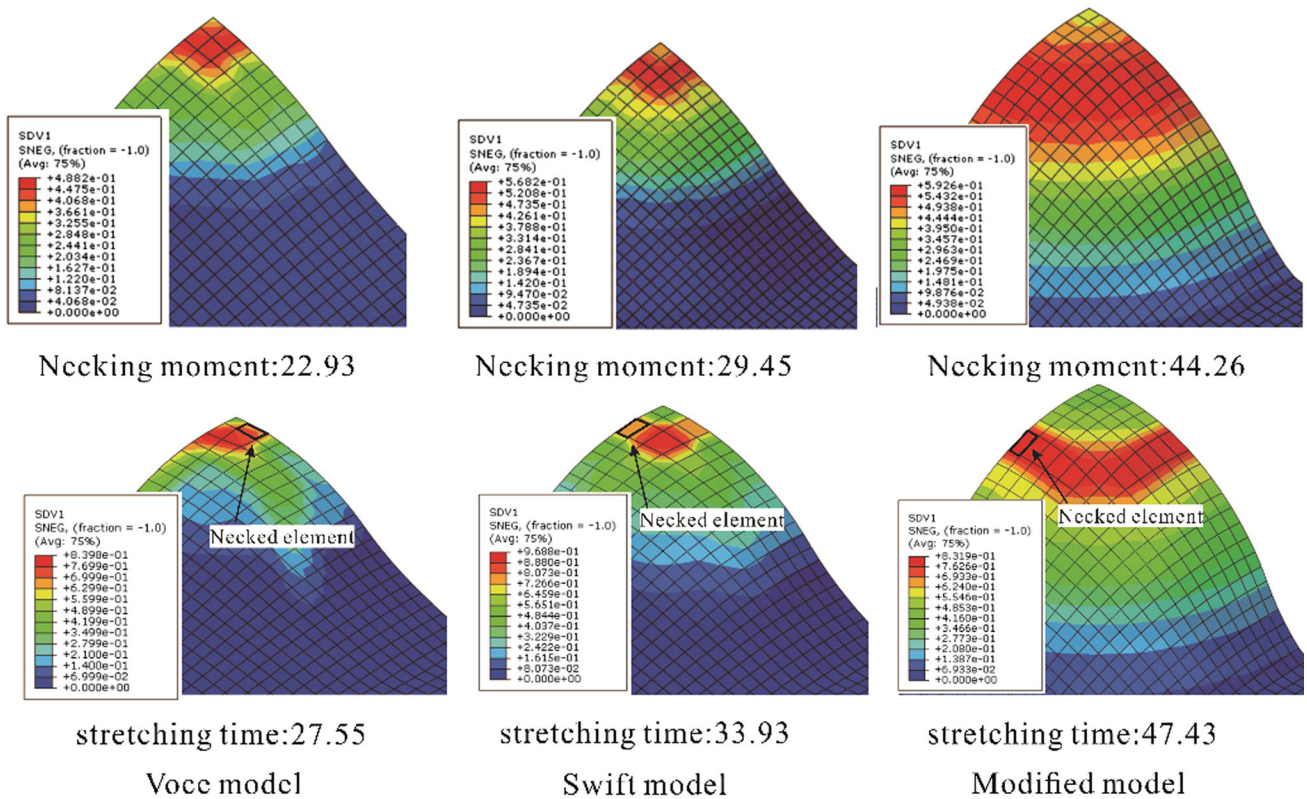


Fig. 19 Necked element under different hardening laws

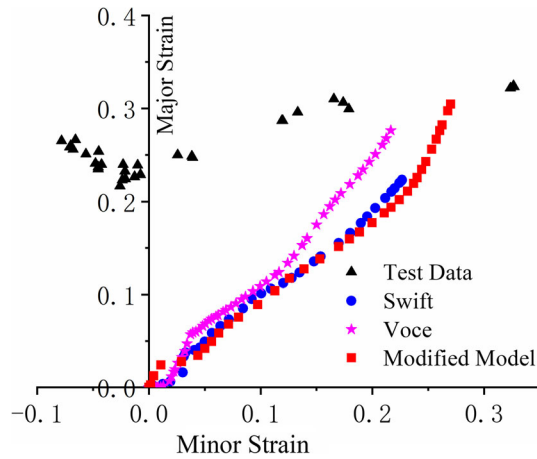


Fig. 20 Simulated strain path and limit strains under different hardening laws

5. Conclusion

In this study, the limit strains of 5754-O aluminum alloy sheets are focused on considering the hardening law effect. The parameters in the four hardening laws investigated were fitted by the uniaxial tensile test and utilized to predict the forming limit by applying the M–K theory and Yld2000-2d yield criterion. After the influence of the hardening law on the predicted results was discussed, a modified LSV model was proposed to predict the FLC with more accuracy and validated by numerically stretching the sheet metal. Thus, the value of the parameter $H = d\sigma_e/d\varepsilon_e$ affected the yield surface evolution in

the M–K approach prediction procedure. Decreasing parameter H caused the strain state in the groove to be close to the plane strain state, and a small limit strain was predicted. The modified LSV hardening law can be used to predict the forming limit of the 5754-O aluminum alloy sheet.

Acknowledgments

This study was supported by a grant from the National Natural Science Foundation of China (No. 52005516) and the Project of the State Key Laboratory of High Performance Complex Manufacturing, Central South University (Nos. ZZYJKT2021-03).

References

1. D.W.A. Rees, Factors influencing the FLD of automotive sheet metal [J], *J. Mater. Process. Technol.*, 2001, **118**(1–3), p 1–8.
2. A. Graf and W. Hosford, The influence of strain-path changes on forming limit diagrams of A1 6111 T4 [J], *Int. J. Mech. Sci.*, 1994, **36**(10), p 897–910.
3. R. Uppaluri, N.V. Reddy and P.M. Dixit, An analytical approach for the prediction of forming limit curves subjected to combined strain paths [J], *Int. J. Mech. Sci.*, 2011, **53**(5), p 365–373.
4. J. Cao, H. Yao, A. Karafilis et al., Prediction of localized thinning in sheet metal using a general anisotropic yield criterion [J], *Int. J. Plast.*, 2000, **16**(9), p 1105–1129.
5. A. Reyes, O.S. Hopperstad, T. Berstad et al., Prediction of necking for two aluminum alloys under non-proportional loading by using an FE-based approach [J], *Int. J. Mater. Form.*, 2008, **1**(4), p 211–232.
6. D. Vysochinskiy, T. Coudert, O.S. Hopperstad et al., Experimental study on the formability of AA6016 sheets pre-strained by rolling [J], *Int. J. Mater. Form.*, 2017, **10**, p 1–17.

7. S. Dhara, S. Basak, S.K. Panda et al., Formability analysis of pre-strained AA5754-O sheet metal using Yld96 plasticity theory: role of amount and direction of uni-axial pre-strain [J], *J. Manuf. Process.*, 2016, **24**, p 270–282.
8. H.J. Kleemola and M.T. Pelkkikangas, Effect of predeformation and strain path on the forming limits of steel [J], *Sheet Metal Industries*, 1977, **64**(6), p 591–592.
9. G. Fang, Q.J. Liu, L.P. Lei et al., Comparative analysis between stress- and strain-based forming limit diagrams for aluminum alloy sheet 1060 [J], *Trans. Nonferr. Metals Soc. China*, 2012, **22**(Suppl 2), p s343–s349.
10. A. Werber, W. Nester, M. Gr Nbaum et al., Assessment of forming limit stress curves as failure criterion for non-proportional forming processes [J], *Prod Eng Res Develop*, 2013, **7**(2–3), p 213–221.
11. S.K. Paul, Path independent limiting criteria in sheet metal forming [J], *J. Manuf. Process.*, 2015, **20**, p 291–303.
12. T.B. Stoughton and X. Zhu, Review of theoretical models of the strain-based FLD and their relevance to the stress-based FLD [J], *Int. J. Plast.*, 2004, **20**(8), p 1463–1486.
13. H. Wang, Y. Yan, M. Wan et al., Experimental investigation and constitutive modeling for the hardening behavior of 5754O aluminum alloy sheet under two-stage loading [J], *Int. J. Solids Struct.*, 2012, **49**(26), p 3693–3710.
14. P. Dasappa, K. Inal and R. Mishra, The effects of anisotropic yield functions and their material parameters on prediction of forming limit diagrams [J], *Int. J. Solids Struct.*, 2012, **49**(25), p 3528–3550.
15. A.B.D. Rocha, A.D. Santos, P. Teixeira et al., Analysis of plastic flow localization under strain paths changes and its coupling with finite element simulation in sheet metal forming [J], *J. Mater. Process. Technol.*, 2009, **209**(11), p 5097–5109.
16. F. Barlat, J.C. Brem, J.W. Yoon et al., Plane stress yield function for aluminum alloy sheets—part 1: theory [J], *Int. J. Plast.*, 2003, **19**(9), p 1297–1319.
17. M.A. Iadicola, T. Foecke and S.W. Banovic, Experimental observations of evolving yield loci in biaxially strained AA5754-O [J], *Int. J. Plast.*, 2008, **24**(11), p 2084–2101.
18. H. Wang, Y. Liu, Z. Chen et al., Investigation of the capabilities of yield functions on describing the deformation behavior of 5754O aluminum alloy sheet under combined loading paths [J], *J Shanghai Jiaotong Univ (Sci)*, 2016, **21**(5), p 562–568.
19. H. Wang, M. Wan, X. Wu et al., The equivalent plastic strain-dependent Yld 2000–2d yield function and the experimental verification [J], *Comput. Mater. Sci.*, 2009, **47**(1), p 12–22.
20. T. Kuwabara, T. Mori, M. Asano et al., Material modeling of 6016-O and 6016-T4 aluminum alloy sheets and application to hole expansion forming simulation [J], *Int. J. Plasticity*, 2016, **93**, p 164.
21. Q.T. Pham, B.H. Lee, K.C. Park et al., Influence of the post-necking prediction of hardening law on the theoretical forming limit curve of aluminium sheets [J], *Int. J. Mech. Sci.*, 2018, **140**, p 521.
22. Q.T. Pham and Y.S. Kim, Identification of the plastic deformation characteristics of AL5052-O sheet based on the non-associated flow rule [J], *Met. Mater. Int.*, 2017, **23**, p 1–10.
23. Z. Gronostajski, The constitutive equations for FEM analysis [J], *J. Mater. Process. Tech.*, 2000, **106**(1), p 40–44.
24. M.C. Butuc, J.J. Gracio and A.B.D. Rocha, A theoretical study on forming limit diagrams prediction [J], *J. Mater. Process. Technol.*, 2003, **142**(3), p 714–724.
25. J. Ding, C. Zhang, X. Chu et al., Investigation of the influence of the initial groove angle in the M-K model on limit strains and forming limit curves [J], *Int. J. Mech. Sci.*, 2015, **98**, p 59–69.
26. Z. Marciniak and K. Kuczynski, Limit strains in the processes of stretch-forming sheet metal [J], *Int. J. Mech. Sci.*, 1967, **9**(9), p 609–620.
27. B.L. Ma, M. Wan, X.J. Li et al., Evaluation of limit strain and temperature history in hot stamping of advanced high strength steels (AHSS) [J], *Int. J. Mech. Sci.*, 2017, **129**, p 607–613.
28. B.L. Ma, M. Wan, X.D. Wu et al., Investigation on forming limit of advanced high strength steels (AHSS) under hot stamping conditions [J], *J. Manuf. Process.*, 2017, **30**, p 320–327.
29. B. Ma, K. Diao, X. Wu et al., The effect of the through-thickness normal stress on sheet formability [J], *J. Manuf. Process.*, 2016, **21**, p 134–140.
30. H. Aretz, A simple isotropic-distortional hardening model and its application in elastic–plastic analysis of localized necking in orthotropic sheet metals [J], *Int. J. Plast.*, 2008, **24**(9), p 1457–1480.
31. K. Yoshida, T. Ishizaka, M. Kuroda et al., The effects of texture on formability of aluminum alloy sheets [J], *Acta Mater.*, 2007, **55**(13), p 4499–4506.
32. R. Chiba, H. Takeuchi, M. Kuroda et al., Theoretical and experimental study of forming-limit strain of half-hard AA1100 aluminium alloy sheet [J], *Comput. Mater. Sci.*, 2013, **77**(3), p 61–71.
33. H. Wang, Y. Yan, F. Han et al., Experimental and theoretical investigations of the forming limit of 5754O aluminum alloy sheet under different combined loading paths [J], *Int. J. Mech. Sci.*, 2017, **133**, p 147.
34. Z.M. Yue, H. Badreddine, T. Dang et al., Formability prediction of AL7020 with experimental and numerical failure criteria [J], *J. Mater. Process. Tech.*, 2015, **218**, p 80–88.
35. D. Banabic, H. Aretz, L. Paraianu et al., Application of various FLD modelling approaches [J], *Modell. Simul. Mater. Sci. Eng.*, 2005, **13**(5), p 759–769.
36. X. Chu, L. Leotoing, D. Guines et al., Temperature and strain rate influence on AA5086 forming limit curves: experimental results and discussion on the validity of the M-K model [J], *Int. J. Mech. Sci.*, 2014, **78**(78), p 27–34.
37. C. Zhang, L. Leotoing, G. Zhao et al., A methodology for evaluating sheet formability combining the tensile test with the M-K model [J], *Mater. Sci. Eng., A*, 2010, **528**(1), p 480–485.
38. W.N. Yuan, M. Wan, X.D. Wu et al., A numerical M-K approach for predicting the forming limits of material AA5754-O [J], *Int. J. Adv. Manuf. Technol.*, 2018, **2**, p 87. <https://doi.org/10.1007/s00170-00018-02332-z>
39. B.L. Ma, M. Wan, Z.Y. Cai et al., Investigation on the forming limits of 5754-O aluminium alloy sheet with the numerical Marciniak-Kuczynski approach [J], *Int. J. Mech. Sci.*, 2018, **142**, p 25.
40. B.L. Ma, M. Wan, Z.G. Liu et al., Experimental and numerical determination of hot forming limit curve of advanced high-strength steel [J], *J. Mater. Eng. Perform.*, 2017, **26**(15), p 1–8.
41. F. Ozturka and D. Leeb, Experimental and numerical analysis of out-of-plane formability test [J], *J. Mater. Process. Tech.*, 2005, **170**(1), p 247–253.
42. S. Zhang, L. Leotoing, D. Guines et al., Calibration of anisotropic yield criterion with conventional tests or biaxial test [J], *Int. J. Mech. Sci.*, 2014, **85**(1–4), p 142–151.
43. O. Hering, F. Kolpak and A.E. Tekkaya, Flow curves up to high strains considering load reversal and damage [J], *Int. J. Mater. Form.*, 2019, **12**(32), p 955–972.
44. J. Chen, Z. Guan, P. Ma, Z. Li and D. Gao, Experimental extrapolation of hardening curve for cylindrical specimens via pre-torsion tension tests, *J. Strain Anal. Eng. Des.*, 2020, **55**(1–2), p 20–30.
45. H. Zhang, S. Coppieters, C. Jiménez-Peña et al., Inverse identification of the post-necking work hardening behaviour of thick HSS through full-field strain measurements during diffuse necking [J], *Mech. Mater.*, 2018, **129**(1), p 361.
46. J. Chen, Z. Guan, J. Xing et al., Methods for measuring friction-independent flow stress curve to large strains using hyperbolic shaped compression specimen, *J. Strain Anal. Eng. Des.*, 2022, **57**(1), p 23–37.
47. Z. Cai, M. Wan, Z. Liu et al., Thermal-mechanical behaviors of dual-phase steel sheet under warm-forming conditions [J], *Int. J. Mech. Sci.*, 2017, **126**, p 79–94.
48. B.L. Ma, M. Wan, H. Zhang et al., Evaluation of the forming limit curve of medium steel plate based on non-constant through-thickness normal stress [J], *J. Manuf. Processes*, 2018, **33**, p 175–183.

Publisher's Note Springer Nature remains neutral with regard to jurisdictional claims in published maps and institutional affiliations.

Springer Nature or its licensor (e.g. a society or other partner) holds exclusive rights to this article under a publishing agreement with the author(s) or other rightsholder(s); author self-archiving of the accepted manuscript version of this article is solely governed by the terms of such publishing agreement and applicable law.